JAAS

ROYAL SOCIETY OF CHEMISTRY

PAPER

View Article Online
View Journal | View Issue

Check for updates

Cite this: J. Anal. At. Spectrom., 2024, 39, 1571

Determination of ultra-trace rare earth elements in olivine by laser ablation-sector field-inductively coupled plasma-mass spectrometry†

Hao Chen,[a] Ming Tang,*[a] Shitou Wu *[b] and Xuanyu Liu[a]

Rare earth elements (REEs) are important geochemical tracers in multiple fields of geochemistry. In this study, we develop a method for precise determination of olivine Eu/Eu* and REE concentrations (down to sub ng g^{-1}) using laser ablation-inductively coupled plasma-mass spectrometry (LA-ICP-MS). Using a Thermo Element XR SF-ICP-MS, we demonstrated that the Jet + H cone combination with the guard electrode under Ar–N_2 plasma (a small amount of N_2 added into carrier gas flow) conditions provides the optimal conditions for measuring ^{147}Sm, ^{153}Eu, and ^{158}Gd. Although the Jet + X cone combination could achieve the highest sensitivity, the usage of the X skimmer cone led to an extremely high oxide formation (ThO^+/Th^+ >30%) and severe inter-element fractionation. Under optimized laser parameters (spot size: 160 μm, ablation frequency: 15 Hz, and energy density: 8 J cm^{-2}) and ICP-MS conditions, detection limits of <0.03 ng g^{-1} are obtainable for most REEs. The accuracy and precision were evaluated using GOR132-G reference glasses and three olivine reference materials (MongOL Sh11-2, 06JY31OL, and 06JY06OL). The analytical accuracy of Eu/Eu* for GOR132-G is within 5% and the precision of Eu/Eu* for olivines is better than 10% (2 RSD). Finally, we report the REE concentration data for five low-REE reference materials (olivine: MongOL Sh11-2, 06JY31OL, and 06JY06OL, orthopyroxene: 06JY34OPX, and powder pellet: DTS-2b-NP), which might be useful for further characterization of these reference materials.

Received 2nd April 2024
Accepted 17th April 2024

DOI: 10.1039/d4ja00122b

rsc.li/jaas

Published on 19 April 2024. Downloaded by Peking University on 6/19/2024 3:57:22 AM.

Introduction

Rare earth element (REE) compositions could serve as valuable indicators of geological processes and thus are of particular interest in geochemistry. For example, REEs of clinopyroxene and garnet in mantle peridotite are used to reflect multistage mantle metasomatism;[1] REEs of mantle-derived mafic magma are important geochemical tracers for unraveling the origin and evolution of the continental lithosphere.[2] Among the REEs, europium is a peculiar one due to its multivalence state (Eu^{2+} and Eu^{3+}) under Earth's redox conditions. Thus, the smoothed REE pattern can be perturbed because Eu could exhibit positive or negative anomalies relative to its neighboring Sm and Gd, which is denoted as Eu anomaly (or Eu/Eu*, calculated by Eu_N/sqrt ($Sm_N \times Gd_N$), where subscript N represents chondrite normalized concentrations). The europium anomaly has various applications in understanding geological processes. For example, Eu/Eu* in zircon has been used to investigate crustal thickness and magma redox conditions.[3,4] However, despite the extensive application of REEs in various minerals, much less attention has been paid to olivine because of their ultra-low concentrations (ranging from ng g^{-1} to sub ng g^{-1}), which cannot be analyzed routinely. Thus, the precise determination of olivine REEs, particularly Eu/Eu* therein is pivotal for further extending the areas of the application of REEs.

Inductively coupled plasma-mass spectrometry (ICP-MS) was initially proposed to determine trace and ultra-trace elements in diverse geological samples, with the advantage of multi-element capability, wide dynamic ranges, and low detection limits.[5–8] In the case of measuring ultra-trace REEs in olivine or ultramafic rocks, many attempts have been made with solution analyses, but the results are questionable because solution ICP-MS as a bulk analytical technique could not efficiently avoid micro inclusions in these minerals.[9–13] The laser ablation sampling strategy allows for *in situ* and rapid analysis at high spatial resolution with lower sample consumption.[14–16] Eggins *et al.*[9] successfully obtained effective Dy, Er, and Yb data of olivine, but they were unable to measure the Eu/Eu* and remaining REEs due to relatively low instrument sensitivity, even though they employed a 200 μm spot size and 50 Hz ablation frequency for laser ablation. More recently, Stead *et al.*[13] used laser ablation-

[a]Key Laboratory of Orogenic Belts and Crustal Evolution, Ministry of Education, School of Earth and Space Sciences, Peking University, Beijing 100871, China. E-mail: mingtang@pku.edu.cn

[b]State Key Laboratory of Lithospheric Evolution, Institute of Geology and Geophysics, Chinese Academy of Sciences, Beijing 100029, China. E-mail: shitou.wu@mail.iggcas.ac.cn

† Electronic supplementary information (ESI) available. See DOI: https://doi.org/10.1039/d4ja00122b

Published on 19 April 2024. Downloaded by Peking University on 6/19/2024 3:57:22 AM.

quadrupole-ICP-MS to determine REEs in olivine from a range of lithologies. Under these conditions, the detection limits typically reached 0.2–0.4 ng g^{-1} for REEs but Sm was still found to fall below the detection limit. Compared with quadrupole ICP-MS, sector field ICP-MS has higher sensitivity, and thus is more suitable for this type of element analysis.[17,18] Therefore, in this study, we use laser ablation coupled with sector field mass spectrometry to measure Eu/Eu* and REEs in olivine.

In order to determine the REEs in olivine using LA-SF-ICP-MS precisely, enhanced instrumental sensitivity is desirable. A well-designed interface is pivotal for enhancing instrumental sensitivity because typically less than 1% of ions could pass through the interface and be analyzed by the mass spectrometer.[17,19–22] As key constituents of the interface, the sample and skimmer cones are critical factors for improving instrumental sensitivity. Different types of sample and skimmer cones have different physical characteristics, such as orifice diameters, external/internal angles, and materials, which strongly influence instrumental performance.[23,24] For the Thermo Element XR and/or Neptune Plus, the high-performance Jet sample cone and X skimmer cone are demonstrated for the signal intensity enhancement of B isotope, S isotope, Sr isotope, Nd isotope, Hf isotope and U–Pb.[25–31] Newman *et al.*[19] suggested that sensitivity enhancement related to cone combination is element-specific. Furthermore, different cone combinations also have different effects on polyatomic formation.[19,32] In addition to cone combinations, the use of the guard electrode (GE) and the addition of N_2 into the central carrier gas (the so-called Ar–N_2 plasma) have also been suggested as important means to increase the sensitivity for specific element/isotope measurement.[29,33–36] However, the effect of these high-performance cones, guard electrode, and plasma conditions (Ar or Ar–N_2) has not been investigated for the REE elements.

In this study, we systematically investigate the effects of cone combinations, guard electrode, and plasma conditions of Ar plasma and Ar–N_2 mixed plasma (a small amount of N_2 was added into the carrier gas flow) on the analytical performance of measurement of ultra-trace REEs, particularly Sm, Eu, and Gd, using LA-SF-ICP-MS. In addition, the effects of laser spot size, ablation frequency as well as laser fluence on instrumental sensitivity were also evaluated. The reliability of the newly developed method was validated by analyzing REEs for multiple olivine, orthopyroxene, and ultramafic powder pellet reference materials.

Experimental methods

Instrumentation

All experiments presented here were conducted using an Element XR SF-ICP-MS (Thermo Fisher Scientific, Bremen, Germany) coupled to a GeoLas HD 193 nm ArF excimer laser ablation system (Coherent, Gottingen, Germany) at the Institute

Table 1 Instrumental operation parameters used for LA-SF-ICP-MS analyses

GeoLas HD ArF excimer laser parameters	
Ablation cell	In-house cell, aerosol dispersion volume <3 cm^3
Wavelength (nm)	193
Laser fluence (J cm^{-2})	8
Pulse duration (ns)	20
Ablation frequency (Hz)	15
Laser spot size (μm)	160
Ablation duration (s)	60
Ablation mode	Spot
Ablation gas flow (L min^{-1})	0.75 (He)
Thermo Fischer Scientific element XR ICP-MS parameters	
RF power (W)	1320
Guard electrode	On/off
Interface cones	Standard sample cone + H skimmer cone Standard sample cone + X skimmer cone Jet sample cone + H skimmer cone Jet sample cone + X skimmer cone
Mass resolution ($m/\Delta m$)	~300
Cool gas flow rate (L min^{-1})	15.00 (Ar)
Auxiliary gas flow rate (L min^{-1})	0.80 (Ar)
Makeup gas flow rate (L min^{-1})	0.95 (Ar)
Enhancement gas flow rate (mL min^{-1})	0, 2 (N_2)
Isotopes measured (m/z) and dwell times (ms)	^{25}Mg (1.1), ^{29}Si (6), ^{31}P (6), ^{43}Ca (1.1), ^{45}Sc (6), ^{51}V (6), ^{53}Cr (6), ^{55}Mn (6), ^{57}Fe (1.1), ^{59}Co (6), ^{60}Ni (6), ^{88}Sr (6), ^{137}Ba (6), ^{139}La (6), ^{140}Ce (6), ^{141}Pr (6), ^{146}Nd (6), ^{147}Sm (35), ^{153}Eu (35), ^{158}Gd (35), ^{159}Tb (6), ^{163}Dy (6), ^{165}Ho (6), ^{166}Er (6), ^{169}Tm (6), ^{173}Yb (6), ^{175}Lu (6), ^{178}Hf (6), ^{232}Th (6), ^{232}Th^{16}O (6)
Scan mode	E-scan
Detection mode	Single secondary electron multiplier in triple mode (pulse counting, analog, and Faraday cup), except ^{25}Mg fixed in Faraday cup mode

 This journal is © The Royal Society of Chemistry 2024

Published on 19 April 2024. Downloaded by Peking University on 6/19/2024 3:57:22 AM.

Table 2 Reference materials and sample characteristics[a]

Name	ARM-3	GOR132-G	MongOL Sh11-2	06JY31OL	06JY06OL	DTS-2b-NP	06JY34OPX	
Matrix	Synthetic andesite glass	Synthetic komatiite glass	Olivine	Olivine	Olivine	Dunite	Orthopyroxene	
Location	—	—	Tariat region, Central Mongolia	Jingyu County, North China	Jingyu County, North China	Twin Sisters Mountain	Jingyu County, North China	
Reference	Wu *et al.*, 2019; 2021	Jochum *et al.*, 2006	Batanova *et al.*, 2019	Tang *et al.*, 2012; Su *et al.*, 2015 Wang *et al.*, 2020	Tang *et al.*, 2012; Su *et al.*, 2015 Wang *et al.*, 2020	—	Tang *et al.*, 2012; Su *et al.*, 2015 Wang *et al.*, 2020	
Characterization technique	SN ICP-MS LA-ICP-MS	SN ICP-MS LA-ICP-MS; EPMS; SIMS	SN-ICP-MS LA-ICP-MS	SN ICP-MS	SN ICP-MS	—	SN ICP-MS	LA-ICP-MS
Rare earth element concentrations ($\mu g\ g^{-1}$)								
La	6.6	0.09	—	0.26	0.21	—	0.26	0.001
Ce	8.0	0.39	—	0.49	0.36	—	0.43	0.003
Pr	5.7	0.09	—	0.06	0.05	—	0.06	0.001
Nd	7.5	0.69	—	0.02	0.19	—	0.27	0.01
Sm	6.0	0.51	—	0.04	0.04	—	0.08	0.02
Eu	5.7	0.26	—	0.003	0.01	—	0.03	0.009
Gd	6.0	1.2	—	0.05	0.03	—	0.1	0.004
Tb	6.6	0.27	—	0.008	0.005	—	0.02	0.01
Dy	6.2	2.2	6	0.05	0.03	—	0.16	0.1
Ho	7.2	0.51	3	0.01	0.006	—	0.04	0.02
Er	6.3	1.6	13	0.04	0.02	—	0.13	0.09
Tm	6.5	0.23	3	0.006	0.004	—	0.02	0.02
Yb	8.9	1.6	29	0.06	0.03	—	0.17	0.1
Lu	6.5	0.24	7	0.01	0.006	—	0.03	0.03

[a] '—' means no information available.

This journal is © The Royal Society of Chemistry 2024

Published on 19 April 2024. Downloaded by Peking University on 6/19/2024 3:57:22 AM.

of Geology and Geophysics, Chinese Academy of Sciences. The Element XR is equipped with a so-called "jet-interface", comprising a Jet sample cone, an X-version skimmer cone and a high-capacity vacuum pump (OnTool Booster 150, Asslar, Germany). Four cone combinations were used in this study, including Standard sample cone + H skimmer cone, Jet sample cone + H skimmer cone, Standard sample cone + X skimmer cone, and Jet sample cone + X skimmer cone. Compared with element 2, element XR has an additional Faraday cup, which increases the linear dynamic range of the instrument to over 10^{12} cps.

Measurements of the olivine/orthopyroxene/powder pellet reference materials were performed using the discrete spot mode. Prior to each analysis, we performed 20 laser pulses pre-ablation to remove surface contamination and make sure ablation sites were away from fractures or inclusions. Helium was used as the ablation gas because of its high thermal conductivity, which will reduce melting at the laser pit and result in small and uniform particles. A T-joint was used to add small amounts of nitrogen to the Ar makeup gas flow. Low mass resolution ($m/\Delta m = 300$) was applied to maximize signal intensity. In order to obtain more robust estimates of the detection limits and improve signal stability, we extend the background counting time and laser ablation time to 40 s and 60 s, respectively, for each analysis. Isotopes measured include ^{25}Mg, ^{29}Si, ^{31}P, ^{43}Ca, ^{45}Sc, ^{51}V, ^{53}Cr, ^{55}Mn, ^{57}Fe, ^{59}Co, ^{60}Ni, ^{88}Sr, ^{137}Ba, ^{139}La, ^{140}Ce, ^{141}Pr, ^{146}Nd, ^{147}Sm, ^{153}Eu, ^{158}Gd, ^{159}Tb, ^{163}Dy, ^{165}Ho, ^{166}Er, ^{169}Tm, ^{173}Yb, ^{175}Lu, ^{178}Hf, ^{232}Th, and ^{232}Th^{16}O. With the purpose of measuring Eu/Eu* precisely, we employ a longer dwell time (35 ms) on ^{147}Sm, ^{153}Eu, and ^{158}Gd to improve the counting statistics of these isotopes. There is only one Faraday cup installed in the instrument, which was used to measure ^{25}Mg because of the high signal intensity (>10^9 cps), while all other isotopes (including ^{29}Si) were measured by SEM, either in pulse counting or analog mode. Detailed instrumentation and experimental conditions are reported in Table 1.

Reference materials and samples

We use reference glass ARM-3 as the calibration reference material,[37,38] while ^{29}Si was chosen as the internal standard. GOR132-G was taken as the quality control reference material.[39] The standard bracketing method was used in which calibration material and monitor reference material were measured at the beginning and the end of each session, and at regular intervals during the session (*e.g.*, after every 5 sample analyses). Element concentration calculation was carried out using Microsoft Excel, which allows manual selection of the most appropriate and the same time interval of the time-resolved analyte signal for both the external standard and samples. Besides, the significant single "spikes" that appeared during the analysis were also being filtered.

Three olivine reference materials (MongOL Sh11-2, 06JY31OL, and 06JY06OL), one pressed powder pellet DTS-2b-NP, and one orthopyroxene 06JY34OPX are available for the measurement of REEs. Information regarding the studied samples is summarized in Table 2. MongOL Sh11-2 was extracted from a fertile mantle lherzolite, which is located at Shavaryn-Tsaram, Tariat region, central Mongolia.[40] The samples with prefixes '06JY' all come from the mantle xenoliths entrained in Cenozoic basalts at Longgang volcanic field, north China.[41] 06JY31OL and 06JY06OL were separated from spinel facies lherzolites with coarse-grained and porphyroclastic textures, whereas 06JY34OPX was separated from a coarse-grained spinel harzburgite with an inequigranular texture and mineral breakdown features.[42] All olivine and orthopyroxene references are optically homogeneous and show no zoning in major elements based on scanning electron microscope (SEM) imaging and EPMA. DTS-2b-NP is a nanoparticle pressed powder pellet of dunite and was collected from the Twin Sisters Mountain. Detailed sample information on the mineral chemistry and petrological context can be found in Batanova *et al.*,[40] Tang *et al.*,[42] and Wang *et al.*[43]

Results and discussion

Effects of cone combinations, guard electrode, and plasma conditions on signal intensity

The signal intensities of ^{147}Sm, ^{153}Eu, and ^{158}Gd for NIST SRM 612 at a spot size of 32 μm as a function of the makeup gas flow rate using four cone combinations under the normal mode (GE-off, Ar plasma) are presented in Fig. 1a–l and are denoted in light gray. Compared to the standard arrangement (Standard sample cone + H skimmer cone), the maximum signal intensities of ^{147}Sm, ^{153}Eu, and ^{158}Gd were all improved by a factor of ~10.2, ~7.1, and ~6.8, respectively, when using the Jet sample cone + H skimmer cone, Standard sample cone + X skimmer cone, and Jet sample cone + X skimmer cone. The signal enhancement by the Jet sample cone could be attributed to its larger orifice diameter compared to the Standard sample cone (1.1 mm *vs.* 1.0 mm). Thus, more ions could pass through the Jet sample cone, leading to higher signal intensity.[19] In addition, it has been hypothesized that the height of the Jet cone is higher than that of the Standard cone, making the cone tip closer to the torch, which also exhibits higher sensitivity.[27,34] As for the skimmer cone, both the H skimmer cone and X skimmer have an orifice diameter of 0.8 mm but differ in geometry. The H skimmer cone has a cylindrical entrance and a trumpet-shaped exit, but the entrance and exit of the X skimmer cone are both trumpet-shaped.[21] The sharper tip of the X skimmer cone could transfer the expansive jet from the sampler orifice more efficiently, thereby increasing the analytical sensitivity. Previous studies suggest that the combination of Jet sample cone + X skimmer cone displays the highest sensitivity under the normal mode.[25,27,29,30] However, none of them investigated the effect of the Jet sample cone + H skimmer cone combination on sensitivity. Besides, the signal enhancement factor using a Jet sample cone combined with an X skimmer cone has been suggested to be negatively correlated with the atomic mass number of the element.[19] Thus, under the normal mode, the signal enhancement for ^{147}Sm, ^{153}Eu and ^{158}Gd may not be optimal when using the Jet sample cone + X skimmer cone, as our results suggest that the

 This journal is © The Royal Society of Chemistry 2024

Published on 19 April 2024. Downloaded by Peking University on 6/19/2024 3:57:22 AM.

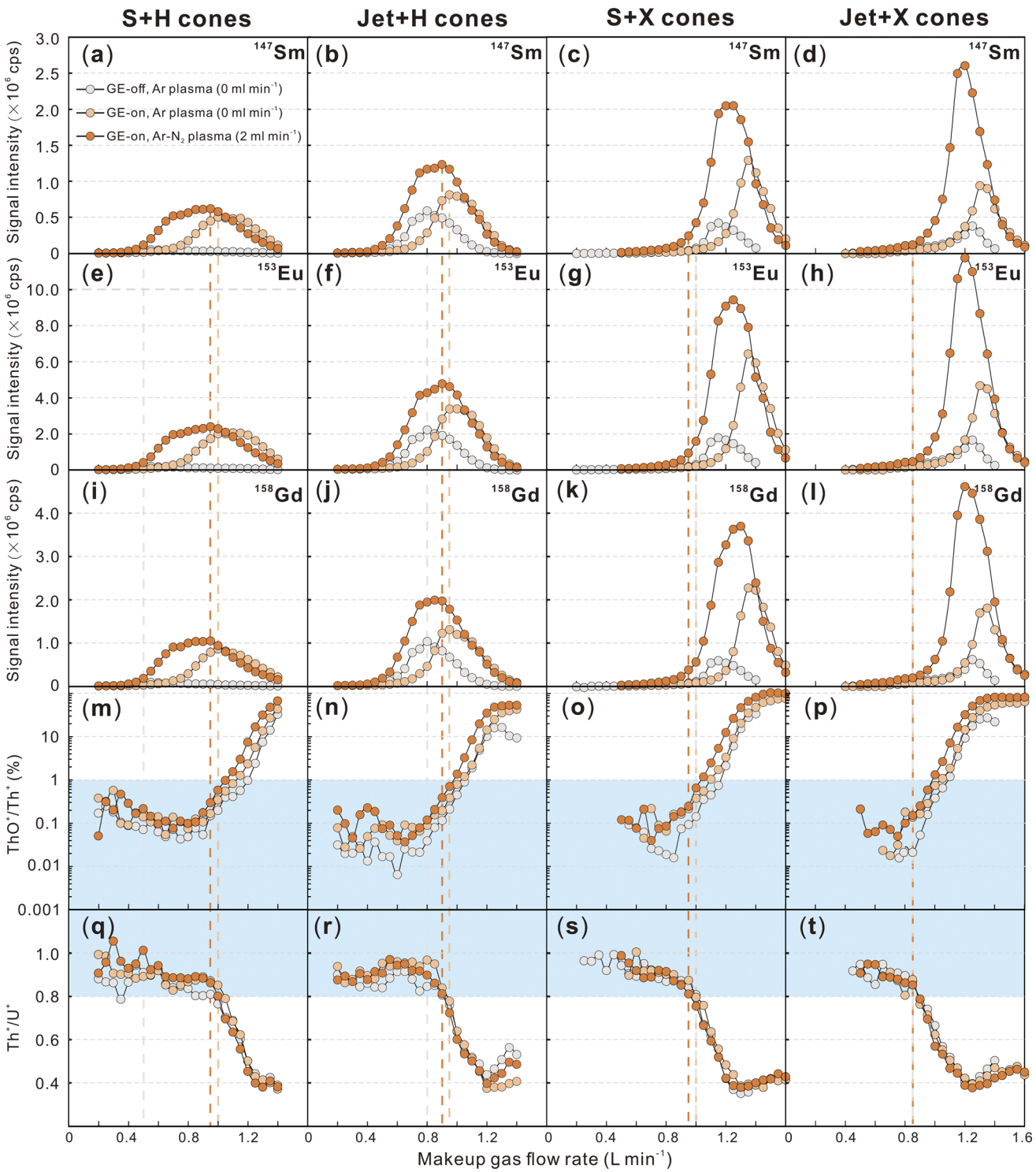


Fig. 1 The integrated average signal intensity of ^{147}Sm, ^{153}Eu, and ^{158}Gd (a–l), ThO^+/Th^+ ratio (m–p), and Th^+/U^+ (q–t) of NIST SRM 612 using a spot size of 32 μm, ablation frequency of 5 Hz and laser fluence of 4 J cm^{-2} for four cone combinations under three different modes (GE-off plus Ar plasma, GE-on plus Ar plasma, and GE-on plus Ar–N_2 plasma). The numbers in parentheses are the N_2 flow rates. The blue bands encompass the range of ThO^+/Th^+ ratio <1.0% and Th^+/U^+ ratio of 0.8–1.2.

signal intensities for ^{147}Sm, ^{153}Eu and ^{158}Gd are higher when combined with those of the Jet sample cone and H skimmer cone.

Signal intensities of ^{147}Sm, ^{153}Eu, and ^{158}Gd as a function of the makeup gas flow rate in the GE-on mode are illustrated in Fig. 1a–l. The signal intensities of ^{147}Sm, ^{153}Eu, and ^{158}Gd all increased in GE-on mode under the four cone combinations,

Published on 19 April 2024. Downloaded by Peking University on 6/19/2024 3:57:22 AM.

although the extent of sensitivity enhancement differs with different cone combinations. Sensitivity enhancement is greatest with the Standard sample cone + H skimmer cone combination. Compared with the GE-off mode, the maximum signal intensities increased by a factor of ~8.8, ~1.4, ~3.5, and ~2.7 for the Standard sample cone + H skimmer cone, Jet sample cone + H skimmer cone, Standard sample cone + X skimmer cone, and Jet sample cone + X skimmer cone combination, respectively. In addition, the optimum makeup gas flow rate (corresponding to the maximum signal intensity) in the GE-on mode is larger than that in the GE-off mode. This is because GE shifts the ionization zone back to the sample cone, which requires a larger makeup gas flow rate to push the ionization zone to the optimum position for compensation. The sensitivity enhancement in GE-on mode should be attributed to the reduced plasma offset, which narrowed the ion energy distribution and enhanced the ion transmission efficiencies during ion extraction processes.[36,44]

It is clear from Fig. 1a–l that adding a small amount of nitrogen could enhance the sensitivity of ^{147}Sm, ^{153}Eu, and ^{158}Gd, regardless of the cone combinations. In the GE-on mode, addition of 2 ml min^{-1} N_2 enhanced the maximum signal intensity for the Standard sample cone + H skimmer cone, Jet sample cone + H skimmer cone, Standard sample cone + X skimmer cone, and Jet sample cone + X skimmer cone combinations by a factor of ~1.2, ~1.5, ~1.6, and ~2.7, respectively. Signal enhancement factors induced by the addition of N_2 are more significant for the X skimmer cone than the H skimmer cone. Furthermore, the optimum makeup gas flow rate decreases with the addition of N_2, which may be caused by a wider axial and more uniform ion distribution after the addition of N_2.[35] Previous studies have found that the signal enhancement factor of N_2 depends on several variables, such as atomic mass number, first ionization energy, and evaporation enthalpy.[27,35,45] The N_2-related signal enhancement may be attributed to the higher thermal conductivity of the Ar–N_2 mixed plasma, which results in better energy transfer in the plasma.[35,46]

Oxide ion formation and elemental fractionation. For LA-SF-ICP-MS measurements, the polyatomic ion interferences and element fractionation would rigorously influence the precision and accuracy of the measured results.[47] In terms of Eu/Eu* analysis, reducing the BaO interference on Eu is of particular importance.[48] Plasma and interface conditions, such as radio frequency power, makeup gas flow rate, and geometry of the sample and skimmer cones are critical factors that control the formation of oxide.[49]

The high-sensitivity Jet sample cone combined with an X skimmer cone suffers from high polyatomic ion interferences (*e.g.*, oxide interference).[19,22] In the normal mode (GE-off plus Ar plasma), the oxide yields are 0.07%, 0.04%, 0.7%, and 17% for the Standard sample cone + H skimmer cone, Jet sample cone + H skimmer cone, Standard sample cone + X skimmer cone, and Jet sample cone + X skimmer cone combinations, respectively. The use of GE could result in higher oxide formation (Fig. 1m–p). The ThO^+/Th^+ ratios in the GE-on mode are 2–47 times as high as those in the GE-off mode for four cone combinations at their corresponding optimum makeup gas flow rates. At the same time, element fractionation becomes more pronounced in the GE-on mode, as indicated by the lower Th^+/U^+ ratios (Fig. 1q–t). Fortunately, addition of N_2 could efficiently reduce the formation of oxide by a factor of 1.2–1.3 for the four cone combinations, which is likely through the competitive formation of NO^+ in the Ar–N_2 plasma.[50] However, addition of N_2 will cause more N-related interferences, which may influence the background intensity of ^{29}Si because of the $^{14}N^{15}N$ interference on ^{29}Si.

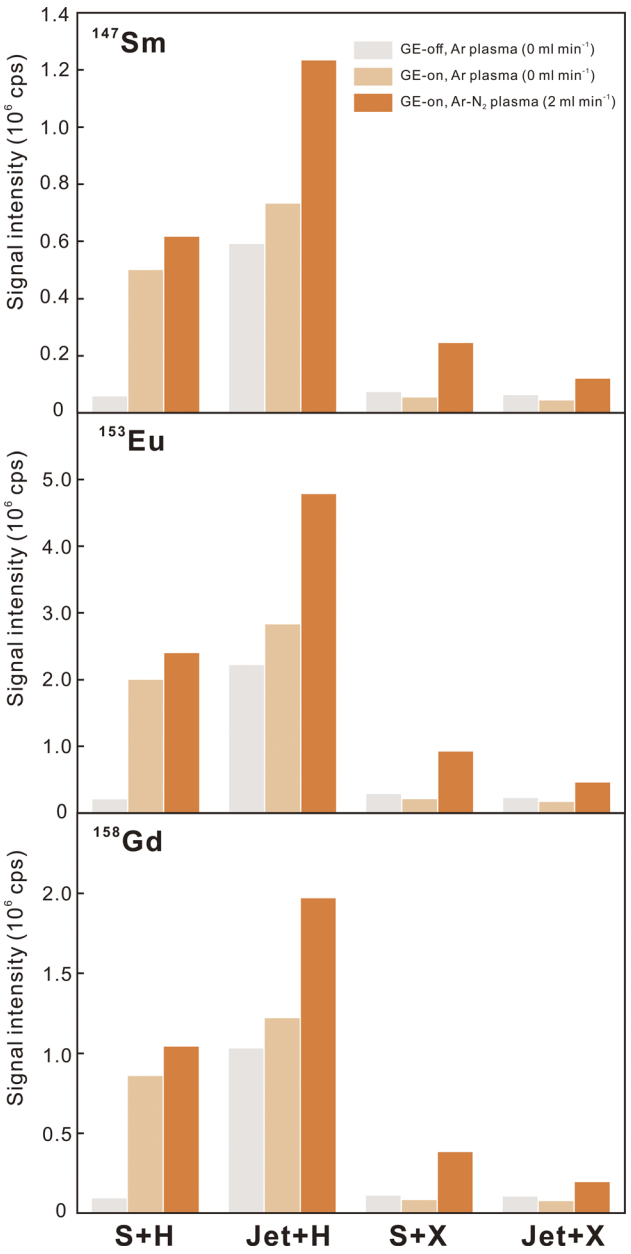


Fig. 2 Maximum signal intensities for ^{147}Sm, ^{153}Eu, and ^{158}Gd of NIST SRM 612 while maintaining a Th^+/U^+ ratio of 0.8–1.2 and a ThO^+/Th^+ ratio of <1.0% using a spot size of 32 μm, ablation frequency of 5 Hz and laser fluence of 4 J cm^{-2} for four cone combinations under three different modes (*i.e.*, GE-off plus Ar plasma, GE-on plus Ar plasma, and GE-on plus Ar–N_2 plasma).

This journal is © The Royal Society of Chemistry 2024

Published on 19 April 2024. Downloaded by Peking University on 6/19/2024 3:57:22 AM.

Nevertheless, our data show that the background intensity for ^{29}Si is still negligible compared to the analyte signal intensity (<1%), which is reasonable for instrumental analysis. Besides, adding nitrogen to the aerosol carrier gas can reduce inter-element fractionation.[51]

Optimal instrumental conditions used for Eu/Eu* measurement. When considering the oxide formation and element fractionation collectively, it can be found that the maximum signal intensities for ^{147}Sm, ^{153}Eu, and ^{158}Gd can be obtained by a Jet sample cone combined with an H skimmer cone with GE-on in the Ar–N_2 plasma (Fig. 2). Under these conditions, the sensitivity for ^{147}Sm, ^{153}Eu, and ^{158}Gd were reduced by ~50–60% compared with the highest sensitivity, but ThO^+/Th^+ was below 1.0% and the Th^+/U^+ ratio ranged between 0.8 and 1.2, which indicate negligible oxide interferences and inter-element fractionation.

Laser ablation parameters used for Eu/Eu* measurement. Appropriate laser parameters could increase signal intensity while reducing fractionation and thus are crucial for accurate and precise determination of REEs and Eu/Eu*. For the laser ablation sampling strategy, the amount of material being swept into the ICP-MS mainly depends on laser spot size, ablation frequency, and laser fluence.[18,52] The simulated results for ^{153}Eu show that signal intensity vary as a function of laser spot size

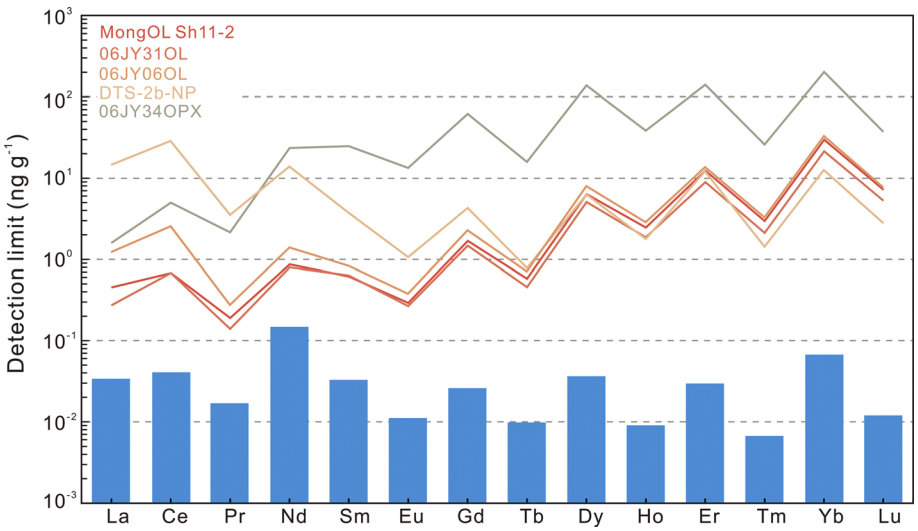


Fig. 3 Bar chart showing the average instrumental detection limit ($n = 50$). Average REE concentrations ($n = 10$) for each reference material are shown for comparison.

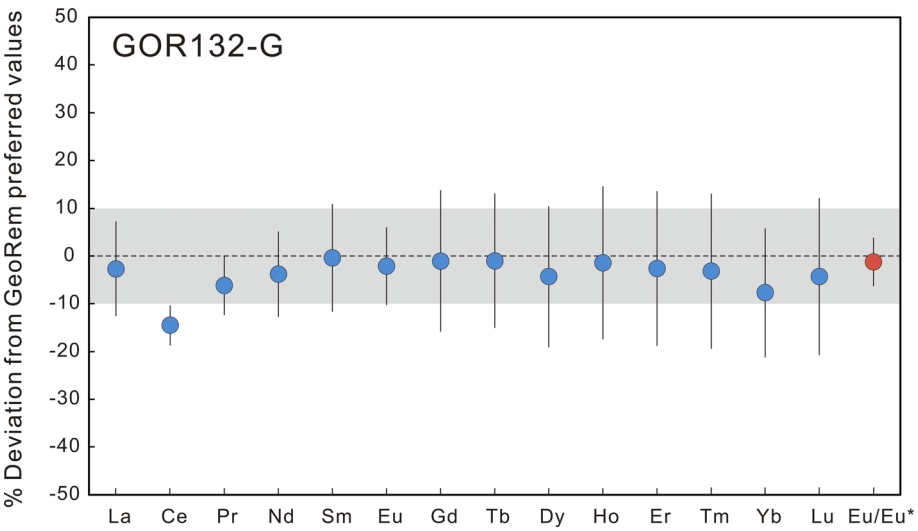


Fig. 4 Relative difference between the measured REE concentrations (blue dots) as well as Eu/Eu* (red dot) and GeoRem preferred values for reference material GOR132-G, which was used as a quality monitor throughout the experiments. Shaded area highlights the ±10% deviation range. Error bars represent 2 SD ($n = 10$).

Published on 19 April 2024. Downloaded by Peking University on 6/19/2024 3:57:22 AM.

and ablation frequency (ESI Fig. S1†). It is clear that ^{153}Eu signal intensity increases with increasing laser spot size and repetition rate. We used a large spot size (160 μm), high ablation frequency (15 Hz), and high laser fluence (8 J cm^{-2}) to analyze the ultra-trace REEs in olivines. Under these laser parameters, the ^{153}Eu signal intensity of olivine MongOL Sh11-2, 06JY31OL, and 06JY06OL is in the range of 105–123 cps, 92–109 cps, and 124–158 cps, respectively. Our measured Eu concentrations generally agreed with the simulated results considering sensitivity drift throughout the measurement. A high laser fluence of 8 J cm^{-2} was chosen here to reduce the matrix effect.[53] Overall, the laser parameters adopted in this study are beneficial for signal enhancement and reduction of fractionation.

Applications to olivine reference materials. Based on the above studies, the Jet sample cone combined with the H skimmer cone with the guard electrode in the Ar–N_2 plasma was selected as the optimal condition for Eu/Eu* measurement. The laser ablation spot size was chosen as 160 μm, the

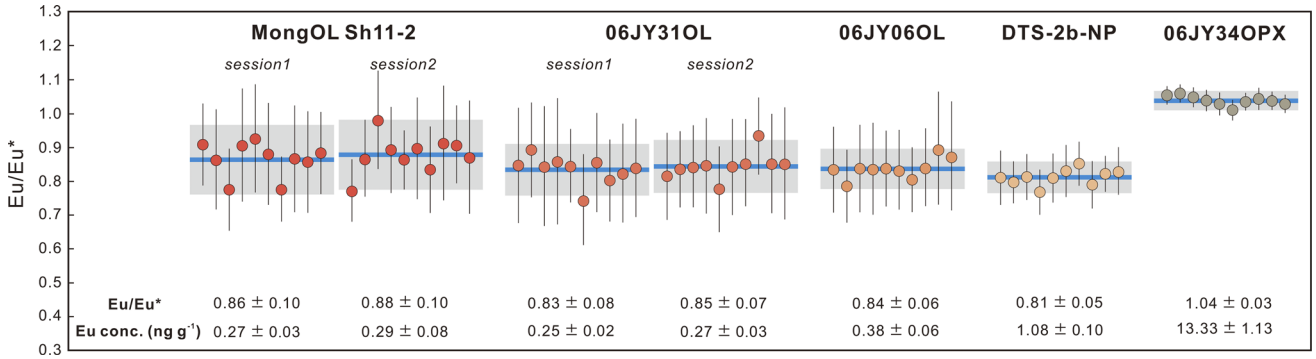


Fig. 5 Repeated analysis ($n = 10$) of Eu/Eu* in five reference materials. Error bars represent the within run precision (2 SE). The blue horizontal lines and gray bands represent the mean and 2 SD values of the measurements, respectively.

Table 3 Measured REE, and minor, and trace element concentrations in reference materials. SiO_2 concentrations used for calibration are also provided here[a]

	MongOL Sh11-2		06JY31OL		06JY06OL		DTS-2b-NP		06JY34OPX	
	$n = 10$		$n = 10$		$n = 10$		$n = 10$		$n = 10$	
	Mean	2 SD	Mean	2 SD	Mean	2 SD	Mean	2 SD	Mean	2 SD
*SiO_2	40.7	0.5	42.2	—	41.5	—	39.4	1.6	57.6	—
La	0.13	0.03	0.21	0.17	0.91	1.87	14.9	1.6	1.6	1.7
Ce	0.30	0.07	0.39	0.20	2.0	4.1	29.4	2.5	5.0	2.6
Pr	0.09	0.04	0.11	0.06	0.24	0.26	3.59	0.33	2.11	0.51
Nd	0.63	0.22	0.71	0.29	1.2	1.1	14.2	2.0	23.5	3.0
Sm	0.55	0.06	0.63	0.11	0.84	0.17	3.77	0.34	24.9	2.5
Eu	0.27	0.03	0.25	0.02	0.38	0.06	1.08	0.10	13.3	1.1
Gd	1.67	0.18	1.47	0.20	2.29	0.29	4.37	0.53	61.8	4.8
Tb	0.59	0.12	0.46	0.08	0.71	0.12	0.79	0.20	15.9	1.3
Dy	6.6	1.3	5.09	0.88	8.02	0.58	6.4	1.3	138	10
Ho	2.55	0.51	1.83	0.31	2.89	0.30	1.81	0.48	38.4	2.5
Er	12.6	1.9	8.9	1.0	13.8	1.2	12.4	1.5	141	10
Tm	3.10	0.46	2.12	0.37	3.31	0.50	1.45	0.32	26.0	2.1
Yb	30.6	3.7	21.3	3.0	33.4	2.3	12.8	2.2	202	8
Lu	7.47	0.91	5.28	0.76	7.81	0.54	2.83	0.53	37.2	2.7
P	69.1	4.1	77.0	5.2	58.5	6.4	6.9	1.1	7.2	1.1
Ca	670	46	876	54	617	53	872	60	5595	640
Sc	3.96	0.28	4.66	0.46	3.64	0.61	4.14	0.25	23.3	1.3
V	6.64	0.06	6.27	0.20	4.22	0.08	25.1	0.7	83.6	3.9
Cr	147	2	208	9	99.5	2.7	16 614	354	3843	179
Mn	1234	20	1197	19	1306	58	891	28	1090	20
Co	155	2	152	2	149	4	113	2	59.4	0.7
Ni	2790	28	2991	33	2662	126	3460	38	748	12

[a] '—' represents no data available. "*SiO_2" shows that the data were collected from the literature and used for internal standardization. Concentration of SiO_2 is given in wt%. From La to Lu element concentrations are given in ng g^{-1}. From P to Ni element concentrations are given in μg g^{-1}.

 This journal is © The Royal Society of Chemistry 2024

Published on 19 April 2024. Downloaded by Peking University on 6/19/2024 3:57:22 AM.

ablation frequency was 15 Hz, and the laser fluence was 8 J cm^{-2}. It should be noted that the laser parameters used in the optimization experiment and olivine analysis are different, which increases the amount of aerosol being introduced into the ICP. This would lead to the plasma loading effect, and the optimum makeup gas flow rate could be slightly shifted (ESI Fig. S2†). However, it is challenging to evaluate this plasma mass loading effect precisely in our measurements for two reasons. Firstly, element XR has a high sensitivity, thus it is not suitable for using large sampling parameters for NIST SRM 612, as it will result in very high signal intensity and may damage the detectors; NIST SRM 614 is a potential candidate, but this material may have a completely different ablation behaviors than that of geological materials because it is almost transparent. Secondly, olivine contains extremely low concentrations of REEs, Th, and U, and thus the weak sensitivity is impractical for this instrument optimization experiment. Despite this, our results (Fig. 3–6) suggest that the method we employed is sufficient to measure the REEs in olivine precisely.

Limits of detection

The limit of detection (LOD) was calculated as the concentration equivalent of three times the standard deviation of the ion counts obtained from the background.[54] The LODs achieved in this study using the LA-SF-ICP-MS technique were typically ~0.03 ng g^{-1}, ~0.01 ng g^{-1}, and ~0.03 ng g^{-1} for Sm, Eu, and Gd, respectively (Fig. 3), and ~0.007–0.148 ng g^{-1} for other REEs. For comparison, the mass fractions measured for Sm, Eu, and Gd in olivine references are generally between 0.55 and 0.85 ng g^{-1}, 0.25–0.35 ng g^{-1}, and 1.45–2.30 ng g^{-1}, respectively, which is at least ~18 times higher than the detection limits for all three elements. Therefore, the LODs are sufficiently low compared to the REE concentrations of the olivine reference materials.

Accuracy

Because all the olivine/orthopyroxene/powder pellet samples in our collection have no certified preferred REE values, we assess the accuracy using the quality monitor reference material GOR132-G. The results show that the measured REE concentrations agree with the GeoRem preferred values within 10% for most of the REEs (Fig. 4). However, Ce is one exception, whose measured concentrations lower then the reference value *ca.* 15% on average. This phenomenon has been previously reported multiple times on GOR132-G.[13,55] Nevertheless, Eu/Eu* of GOR132-G exhibits excellent agreement with the preferred value, with a bias of −1.2% ± 5.1% (2 SD).

Eu/Eu* values of the olivine/orthopyroxene/powder pellet reference materials

The BaO interference on Eu is negligible for olivine and orthopyroxene because of the low oxide yield (ThO^+/Th^+ <1.0%) and low Ba/Eu ratio for these two minerals. However, the Ba/Eu ratio for the ultramafic powder pellet DTS-2b-NP is above 10 000, which may cause significant interference with the Eu measurement and lead to inaccurate results.[48] Despite this, several pieces of evidence suggest that our measured Eu/Eu* in DTS-2b-NP is unlikely to be compromised by BaO interference. First, our measured Eu/Eu* generally agrees with the previously published Eu/Eu* value for the reference sample DTS-2,[11,56,57] which has the same source as DTS-2b-NP. Secondly, there is no correlation between measured Ba concentration and Eu concentration or Eu/Eu* for DTS-2b-NP, indicating that the BaO interference on Eu is trivial.

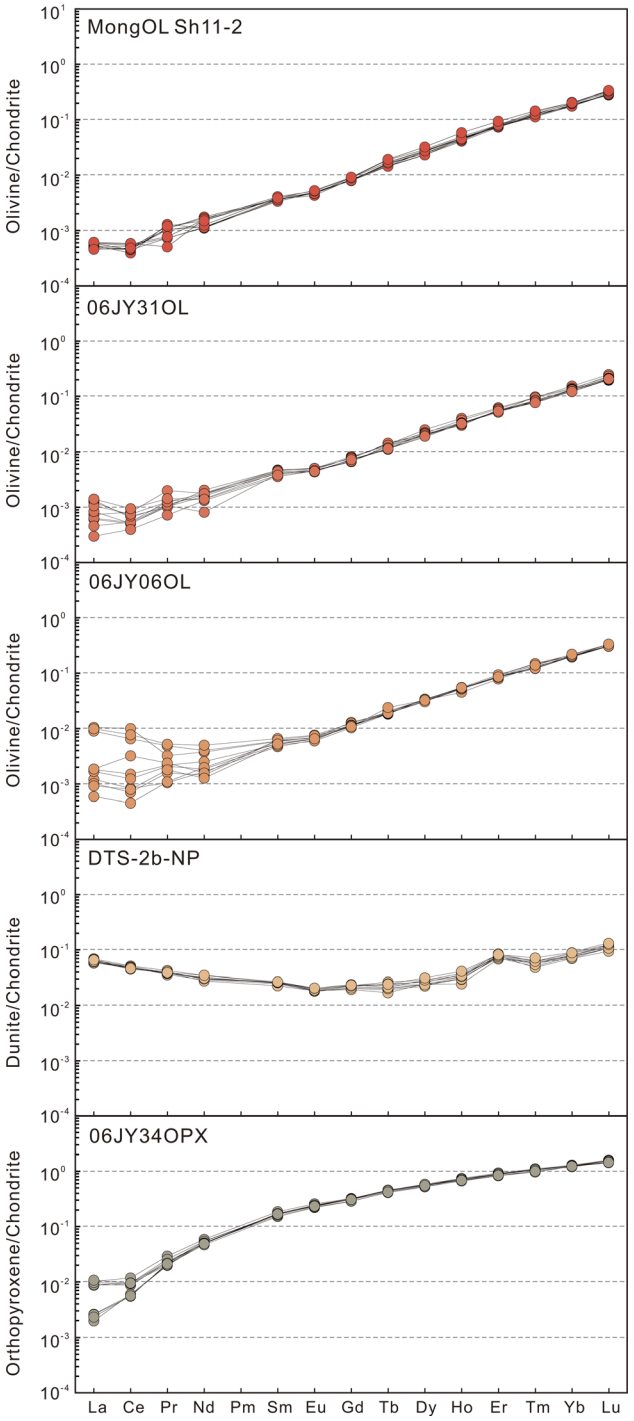


Fig. 6 Chondrite normalized[59] REE patterns for the measured olivine/orthopyroxene/ultramafic powder pellet reference materials.

Published on 19 April 2024. Downloaded by Peking University on 6/19/2024 3:57:22 AM.

Fig. 5 displays the measured Eu/Eu* for five reference materials. The reproducibility of Eu/Eu* was evaluated through replicate measurements ($n = 10$) on five reference materials. The analytical precision is presented as 2 RSD (%). Limited by the ablation site left of reference samples available, we only performed one set of experiments on 06JY06OL, DTS-2b-NP, and 06JY34OPX, while two sets of experiments were performed for MongOL Sh11-2 and 06JY31OL. Repeated analyses of MongOL Sh11-2 yielded an average Eu/Eu* of 0.86 ± 0.10 (2 RSD = 12%) and 0.88 ± 0.10 (2 RSD = 12%). Repeated analyses of 06JY31OL yielded an average Eu/Eu* of 0.83 ± 0.08 (2 RSD = 9%) and 0.85 ± 0.07 (2 RSD = 9%). Repeated analyses of 06JY06OL, 06JY34OPX, and DTS-2b-NP yielded an average Eu/Eu* of 0.84 ± 0.06 (2 RSD = 7%), 0.81 ± 0.05 (2 RSD = 6%), and 1.04 ± 0.03 (2 RSD = 3%), respectively. Except for olivine MongOL Sh11-2, 2 RSD of all other reference materials are below 10%. The slightly higher 2 RSD of olivine MongOL Sh11-2 may be caused by the more heterogeneous Eu/Eu* than those of 06JY31OL and 06JY06OL.

REE concentrations of the olivine/orthopyroxene/powder pellet reference materials

Our measured REE, and minor and trace element concentrations of the olivine/orthopyroxene/powder pellet reference materials are listed in Table 3 and the chondrite normalized REE patterns are shown in Fig. 6. For the olivines and orthopyroxene, it is clear that the LREE concentrations are significantly lower than those of the HREEs. This is in accordance with the lattice strain model predictions, which indicate that the LREEs are more incompatible than HREEs in the olivine/orthopyroxene crystal lattice due to their larger ionic radii.[58] Because the detection limits are low enough compared with the measured concentrations, the more scattered concentrations of LREEs (La to Nd) observed in these olivine and orthopyroxene reference materials may reflect the intra/inter-granular heterogeneities.

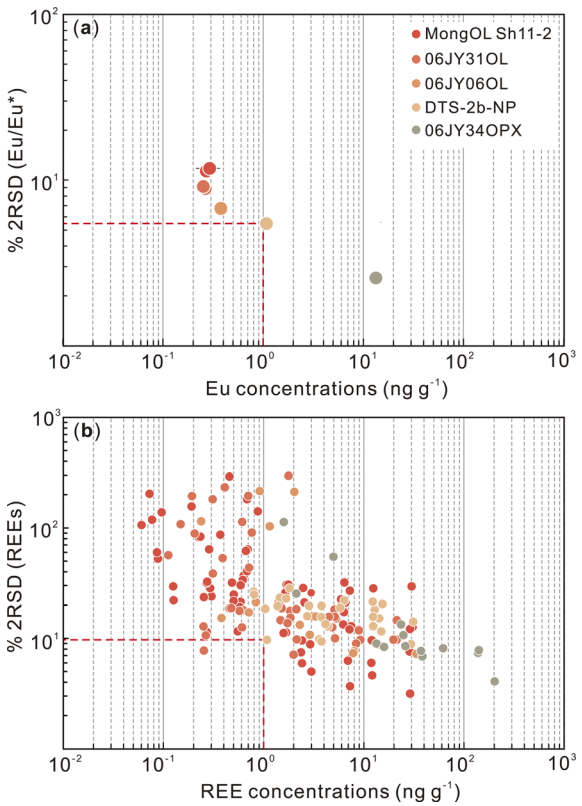


Fig. 7 Correlation between 2 RSD of Eu/Eu* and measured Eu concentrations (a), and correlation between 2 RSD of REEs and measured REE concentrations (b). Horizontal error bars in (a) represent 2 SD (most are smaller than the symbols).

Analytical precision *versus* element concentration

Analytical precision improves with concentration based on counting statistics of signal intensity. Fig. 7a shows the 2RSD of Eu/Eu* *versus* measured Eu concentrations, and Fig. 7b indicates the 2 RSD of REEs *versus* measured REE concentrations for the olivine, orthopyroxene, and ultramafic powder pellet reference materials. It can be found in both panels of Fig. 7 that the 2 RSD exponentially negatively correlates with concentration. The relatively large scatter may in part result from the heterogeneous compositions of the REEs, particularly the LREEs, which are more readily influenced by mantle metasomatism because of their extremely low concentrations in olivine and orthopyroxene. Nevertheless, the 2 RSD for Eu/Eu* and REE concentrations are generally below 10% for elements whose concentrations are above 1 ng g^{-1}. Therefore, we suggest that the protocol adopted in this study could be used to precisely determine the Eu/Eu* and other REEs at the ng g^{-1} level.

Conclusions

The results presented in this study demonstrate that sample and skimmer cone combination, guard electrode, and plasma conditions are critical for improving instrument performance of LA-SF-ICP-MS for Eu/Eu* analysis. Considering sensitivity, oxide formation, and inter-element fractionation collectively, the combination of the Jet sample cone + H simmer cone with the guard electrode in the Ar–N_2 mixed plasma (2 ml min^{-1} N_2) was chosen as the optimal instrumental condition. As for laser parameters, 160 μm laser spot size, 15 Hz repetition rate, and 8 J cm^{-2} laser fluence are favorable for both high sensitivity as well as subdued element fractionation. Under these optimized conditions, the Sm, Eu, and Gd in olivine, orthopyroxene, and ultramafic pellets could be measured effectively. The detection limits of <0.03 ng g^{-1} are obtainable for most RREs. To our knowledge, this is the firstreported such detection capability. The 2 RSD values of repeated measurements of Eu/Eu* in the olivine/orthopyroxene/powder pellet reference materials are generally less than 10%. We suggest that the analytical method presented here provides a reliable means for determining the ng g^{-1} level of Eu/Eu* and REE concentrations in olivine by LA-SF-ICP-MS.

This journal is © The Royal Society of Chemistry 2024

Published on 19 April 2024. Downloaded by Peking University on 6/19/2024 3:57:22 AM.

Conflicts of interest

There are no conflicts to declare.

Acknowledgements

We would like to thank Valentina G. Batanova and Benxun Su for providing the reference materials analyzed in this study. Besides, Hongxia Ma, Lei Xu, Junlong Niu, Kangshi Hou, Ziyi Guo, and Zi Ye are thanked for their assistance in the experiments. This research was financially supported by the National Natural Science Foundation of China (grants 42125302, 42073026, 41888101, and 42273034). M. T. is grateful for the support from the New Cornerstone Science Foundation through the XPLORER PRIZE.

References

1 S. Y. O'Reilly and W. Griffin, *Metasomatism and the Chemical Transformation of Rock*, 2013, pp. 471–533.
2 D. Pearson and N. Wittig, *J. Geol. Soc.*, 2008, **165**, 895–914.
3 M. Tang, W.-Q. Ji, X. Chu, A. Wu and C. Chen, *Geology*, 2021, **49**, 76–80.
4 D. Trail, E. B. Watson and N. D. Tailby, *Geochim. Cosmochim. Acta*, 2012, **97**, 70–87.
5 J. S. Becker, *Spectrochim. Acta, Part B*, 2002, **57**, 1805–1820.
6 S. Becker, *Inorganic Mass Spectrometry: Principles and Applications*, John Wiley & Sons, 2008.
7 N. H. Bings, A. Bogaerts and J. A. Broekaert, *Anal. Chem.*, 2010, **82**, 4653–4681.
8 C. Engelhard, *Anal. Bioanal. Chem.*, 2011, **399**, 213–219.
9 S. Eggins, R. Rudnick and W. McDonough, *Earth Planet. Sci. Lett.*, 1998, **154**, 53–71.
10 A. Makishima and E. Nakamura, *Geostand. Geoanal. Res.*, 2006, **30**, 245–271.
11 K. Nakamura and Q. Chang, *Geostand. Geoanal. Res.*, 2007, **31**, 185–197.
12 M. Rospabé, M. Benoit and F. Candaudap, *Geostand. Geoanal. Res.*, 2018, **42**, 115–129.
13 C. V. Stead, E. L. Tomlinson, B. S. Kamber, M. G. Babechuk and C. A. McKenna, *Geostand. Geoanal. Res.*, 2017, **41**, 197–212.
14 D. Günther, R. Frischknecht, C. A. Heinrich and H.-J. Kahlert, *J. Anal. At. Spectrom.*, 1997, **12**, 939–944.
15 D. Günther and B. Hattendorf, *TrAC, Trends Anal. Chem.*, 2005, **24**, 255–265.
16 R. E. Russo, X. Mao, H. Liu, J. Gonzalez and S. S. Mao, *Talanta*, 2002, **57**, 425–451.
17 C. Latkoczy and D. Günther, *J. Anal. At. Spectrom.*, 2002, **17**, 1264–1270.
18 M. Petrelli, K. Laeger and D. Perugini, *Geosci. J.*, 2016, **20**, 851–863.
19 K. Newman, P. A. Freedman, J. Williams, N. S. Belshaw and A. N. Halliday, *J. Anal. At. Spectrom.*, 2009, **24**, 742–751.
20 J. M. Cottle, A. J. Burrows, A. Kylander-Clark, P. A. Freedman and R. S. Cohen, *J. Anal. At. Spectrom.*, 2013, **28**, 1700–1706.
21 M. He, Z. Jin, H. Lu, L. Deng and C. Luo, *Int. J. Mass Spectrom.*, 2016, **408**, 33–37.
22 K. Newman, *J. Anal. At. Spectrom.*, 2012, **27**, 63–70.
23 D. Günther, H. P. Longerich, S. E. Jackson and L. Forsythe, *Fresenius' J. Anal. Chem.*, 1996, **355**, 771–773.
24 C. Bouman, M. Deerberg, J. Schwieters and T. Scientific, *Application Note*, 2009, 30187.
25 L. Lin, Z. Hu, L. Yang, W. Zhang, Y. Liu, S. Gao and S. Hu, *Chem. Geol.*, 2014, **386**, 22–30.
26 W. Zhang, Z. Hu, Y. Liu, T. Wu, X. Deng, J. Guo and H. Zhao, *Chem. Geol.*, 2018, **479**, 10–21.
27 Z. Hu, Y. Liu, S. Gao, W. Liu, W. Zhang, X. Tong, L. Lin, K. Zong, M. Li and H. Chen, *J. Anal. At. Spectrom.*, 2012, **27**, 1391–1399.
28 S. Wu, Y. Yang, N. M. Roberts, M. Yang, H. Wang, Z. Lan, B. Xie, T. Li, L. Xu and C. Huang, *Sci. China: Earth Sci.*, 2022, **65**, 1146–1160.
29 L. Xu, Z. Hu, W. Zhang, L. Yang, Y. Liu, S. Gao, T. Luo and S. Hu, *J. Anal. At. Spectrom.*, 2015, **30**, 232–244.
30 J. Fu, Z. Hu, W. Zhang, L. Yang, Y. Liu, M. Li, K. Zong, S. Gao and S. Hu, *Anal. Chim. Acta*, 2016, **911**, 14–26.
31 S. Wu, M. Yang, Y. Yang, L. Xie, C. Huang, H. Wang and J. Yang, *Int. J. Mass Spectrom.*, 2020, **456**, 116394.
32 N. Zahran, A. Helal, M. Amr, A. Abdel-Hafiez and H. Mohsen, *Int. J. Mass Spectrom.*, 2003, **226**, 271–278.
33 P. K. Appelblad, I. Rodushkin and D. C. Baxter, *J. Anal. At. Spectrom.*, 2000, **15**, 359–364.
34 T. He, Q. Ni, Q. Miao and M. Li, *J. Anal. At. Spectrom.*, 2018, **33**, 1021–1030.
35 Z. Hu, S. Gao, Y. Liu, S. Hu, H. Chen and H. Yuan, *J. Anal. At. Spectrom.*, 2008, **23**, 1093–1101.
36 S. Wu, Y. Yang, H. Wang, C. Huang, L. Xie and J. Yang, *At. Spectrosc.*, 2020, **41**, 154–161.
37 S. Wu, G. Wörner, K. P. Jochum, B. Stoll, K. Simon and A. Kronz, *Geostand. Geoanal. Res.*, 2019, **43**, 567–584.
38 S. Wu, Y. Yang, K. P. Jochum, R. L. Romer, J. Glodny, I. P. Savov, S. Agostini, J. C. De Hoog, S. T. Peters and A. Kronz, *Geostand. Geoanal. Res.*, 2021, **45**, 719–745.
39 K. P. Jochum, B. Stoll, K. Herwig, M. Willbold, A. W. Hofmann, M. Amini, S. Aarburg, W. Abouchami, E. Hellebrand and B. Mocek, *Geochem., Geophys., Geosyst.*, 2006, **7**, 1–44.
40 V. G. Batanova, J. M. Thompson, L. V. Danyushevsky, M. V. Portnyagin, D. Garbe-Schönberg, E. Hauri, J. I. Kimura, Q. Chang, R. Senda and K. Goemann, *Geostand. Geoanal. Res.*, 2019, **43**, 453–473.
41 B. X. Su, X. Y. Gu, E. Deloule, H. F. Zhang, Q. L. Li, X. H. Li, N. Vigier, Y. J. Tang, G. Q. Tang and Y. Liu, *Geostand. Geoanal. Res.*, 2015, **39**, 357–369.
42 Y.-J. Tang, H.-F. Zhang, E. Deloule, B.-X. Su, J.-F. Ying, Y. Xiao and Y. Hu, *Lithos*, 2012, **149**, 79–90.
43 W. Jing, S. BenXun, T. GuoQiang, G. BingYu, W. ShiTou and L. Jiao, *Acta Petrol. Sin.*, 2020, **36**, 1274–1284.
44 B. Duersch, *J. Anal. At. Spectrom.*, 1999, **14**, 615–619.
45 J. Yu, H. Zhao, T. He, T. Luo, W. Zhang, K. Zong, J. Lin, Y. Liu and Z. Hu, *J. Anal. At. Spectrom.*, 2021, **36**, 723–732.

Published on 19 April 2024. Downloaded by Peking University on 6/19/2024 3:57:22 AM.

46 G. L. Scheffler and D. Pozebon, *J. Anal. At. Spectrom.*, 2015, **30**, 468–478.
47 S. Aries, M. Valladon, M. Polvé and B. Dupré, *Geostand. Newsl.*, 2000, **24**, 19–31.
48 A. J. Kent, *J. Anal. At. Spectrom.*, 2005, **20**, 1256–1262.
49 K. Itano and T. Iizuka, *J. Anal. At. Spectrom.*, 2017, **32**, 2003–2010.
50 G. Scheffler and D. Pozebon, *Anal. Methods*, 2014, **6**, 6170–6182.
51 C. Agatemor and D. Beauchemin, *Anal. Chim. Acta*, 2011, **706**, 66–83.
52 F. E. Jenner and H. S. C. O'Neill, *Geochem., Geophys., Geosyst.*, 2012, **13**, 1–17.
53 E. F. Cromwell and P. Arrowsmith, *Anal. Chem.*, 1995, **67**, 131–138.
54 H. Longerich, S. Jackson and D. Gunther, *J. Anal. At. Spectrom.*, 1996, **11**, 899–904.
55 S. Gibson, S. McMahon, J. Day and J. Dawson, *J. Petrol.*, 2013, **54**, 1503–1546.
56 I. Raczek, B. Stoll, A. W. Hofmann and K. Peter Jochum, *Geostand. Newsl.*, 2001, **25**, 77–86.
57 M. Ulrich, S. Bureau, C. Chauvel and C. Picard, *Geostand. Geoanal. Res.*, 2012, **36**, 7–20.
58 B. Wood and J. Blundy, in *Treatise on Geochemistry*, Elsevier, Oxford, 2014, pp. 421–448.
59 W. F. McDonough and S.-S. Sun, *Chem. Geol.*, 1995, **120**, 223–253.

This journal is © The Royal Society of Chemistry 2024